
NUMERICALLY CONSISTENT NON-BOUSSINESQ SUBGRID-SCALE STRESS MODEL WITH ENHANCED CONVERGENCE

Yuenong Ling^{1,*} and Adrian Lozano-Duran^{1,2}

¹Department of Aeronautics and Astronautics, Massachusetts Institute of Technology, Cambridge, USA

²Graduate Aerospace Laboratories, California Institute of Technology, Pasadena, USA

* Author to whom any correspondence should be addressed.

January 29, 2026

ABSTRACT

We extend the data-assimilation approach of Ling and Lozano-Duran (2025) to develop machine-learning-based subgrid-scale stress (SGS) models for large-eddy simulation (LES) that are consistent with the numerical scheme of the flow solver. The method accounts for configurations with two inhomogeneous directions and is applied to turbulent boundary layers (TBL) under adverse pressure gradients (APG). To overcome the limitations of linear eddy-viscosity closures in complex flows, we adopt a non-Boussinesq SGS formulation along with a dissipation-matching training loss. A second improvement is the integration of a multi-task learning strategy that explicitly promotes monotonic convergence with grid refinement, a property that is often absent in conventional SGS models. *A posteriori* tests show that the proposed model improves predictions of the mean velocity and wall-shear stress relative to the Dynamic Smagorinsky model (DSM), while also achieving monotonic convergence with grid refinement.

1 Introduction

Wall-modeled large-eddy simulation (WMLES) has emerged as a popular tool for high-Reynolds-number flow simulations in industrial applications, offering a favorable balance between accuracy and computational efficiency compared to direct numerical simulation (DNS) and wall-resolved large-eddy simulation (WRLES) (Kawai and Larsson, 2012; Bose and Park, 2018; Mani and Dorgan, 2023). In this framework, SGS models are employed to account for the effects of unresolved small-scale eddies, while wall models are used to bypass the prohibitive cost of resolving near-wall motions.

Conventional SGS models typically rely on physical approximations and empirical parameter tuning (Jimenez and Moser, 1998; Sagaut, 2006). These approaches are often limited by their underlying assumptions, which can lead to significant inaccuracies in complex flow scenarios (Goc et al., 2021b; Agrawal et al., 2022; Hu et al., 2023; Hayat and Park, 2024). A related limitation is the common practice of developing wall and SGS closures as separate components, which can introduce inconsistencies and compounding errors in WMLES (Ling et al., 2022; Arranz et al., 2024). In addition, discretization errors are frequently neglected when coarse grids are used in practical simulations, further degrading predictive accuracy (Bae and Lozano-Durán, 2017; Lozano-Durán and Bae, 2019; Goc, 2023; Lozano-Durán and Bae, 2023). Finally, a persistent challenge in WMLES is non-monotonic grid convergence of the solution (Larsson et al., 2016; Lozano-Durán and Bae, 2019). This issue often stems from the interplay between SGS modeling and numerical errors (Lozano-Durán and Bae, 2019; Lozano-Durán et al., 2022; Hu et al., 2024), which can cause predictions to deteriorate even as the mesh is refined.

While machine-learning-based (ML-based) SGS models have been developed to address the limitations of conventional closures (Duraisamy, 2021; Sanderse et al., 2025; Choi et al., 2025), early attempts often underperformed in *a posteriori* tests, especially on the coarse grids typical of WMLES. This is primarily because they focused on *a priori* training

using filtered or coarsened high-fidelity DNS data (Gamahara and Hattori, 2017; Xie et al., 2019; Maulik et al., 2019; Park and Choi, 2021; Liu et al., 2022; Kang et al., 2023; Kim et al., 2024; Yang et al., 2024; Li et al., 2025). However, it is well established that success in *a priori* testing is only weakly correlated with *a posteriori* performance because filtered DNS data are generally inconsistent with LES, except under very specific conditions (Lund, 2003; Bae and Lozano-Durán, 2017, 2018; Bae and Lozano-Duran, 2022; Huang et al., 2025). For this reason, recent efforts have shifted toward *a posteriori* training strategies.

A posteriori training integrates the SGS model directly into the WMLES solver at the target grid resolution, explicitly accounting for numerical errors and ensuring consistency between training and deployment. However, adoption has been slow due to the substantial algorithmic and implementation complexity of these methods. Proposed approaches include adjoint-based methods (MacArt et al., 2021; Sirignano and MacArt, 2023; Yuan et al., 2023), ensemble-based data assimilation (Mons et al., 2021; Wang et al., 2023), differentiable solvers (List et al., 2022; Shankar et al., 2025; Fan et al., 2026), reinforcement learning (Novati et al., 2021; Kim et al., 2022; Beck and Kurz, 2023; Kurz et al., 2025), probabilistic models (Ephrati, 2025), continuous data assimilation (Ephrati et al., 2025), and the τ -orthogonal method (Hoekstra et al., 2024; Hoekstra and Edeling, 2026). Despite their promise, widespread application remains limited by high computational cost and the difficulty of integrating these techniques into production WMLES solvers.

To date, a compelling ML-based SGS model leveraging data assimilation (at least in terms of demonstrated applicability) is the building-block flow model (BFM) proposed by Ling et al. (2022) and Arranz et al. (2024). This framework jointly learns an SGS closure and a wall model. The SGS component is formulated as an optimization problem that matches DNS statistics under a prescribed numerical scheme. The model trained via this approach has demonstrated good performance across a broad range of configurations, from canonical turbulent channel flows and pipes to more complex geometries such as the Gaussian bump, the NASA Juncture Flow, and the Common Research Model. However, the original BFM data-assimilation method is restricted to configurations with only one inhomogeneous direction, and it was also reported that certain datasets involving separated flows could not be assimilated.

To address these challenges, Ling and Lozano-Duran (2025) proposed a cost-effective data-assimilation-based approach for SGS modeling for developing improved versions of the BFM. The method generates training data using statistically nudged WMLES, in which a nudging term drives the simulation toward prescribed target statistics. A multiple-instance learning strategy is then used to regress the SGS model against the resulting nudging forcing. In this paper, we extend this framework to TBLs subject to APG, a configuration with two inhomogeneous directions. To accommodate the richer physics, we generalize the model from a scalar eddy-viscosity closure to a non-Boussinesq tensorial SGS formulation, which has been shown to perform well in complex flows (Moin, 1993; Lozano-Durán and Arranz, 2022; Agrawal et al., 2022). During training, we also enforce constraints on model dissipation, a statistical requirement for SGS closures (Meneveau, 1994; Moser et al., 2021) that has been shown to be essential for capturing smooth-body separation (Iyer and Malik, 2024). Finally, we demonstrate improved grid-refinement behavior, with enhanced convergence properties of the resulting SGS model.

The paper is organized as follows. Section 2 describes the APG TBL case used for training and testing, the nudging approach for flows with two inhomogeneous directions, and the SGS model and machine learning formulation. Section 3 presents the *a posteriori* results and evaluates the effectiveness of the convergence-enhancement strategy. Finally, Section 4 discusses future improvements, and Section 5 concludes the paper.

2 Methods

The procedure for constructing the SGS model consists of three main steps as shown in Figure 1:

1. *Reference DNS statistics*: We extract the mean velocity profile from a DNS of a TBL under APG, which serves as the training target.
2. *Training-data generation via nudging*: We run statistically nudged WMLES in the deployment solver to generate a numerically consistent target forcing that the SGS model must reproduce.
3. *Model training*: We train the SGS model via supervised learning by minimizing a combined loss that matches the mean target forcing and the SGS dissipation obtained from the nudged simulations in step 2.

This approach enables computationally efficient supervised training of the SGS model while retaining key benefits typically associated with (costly) reinforcement learning, such as consistency with the solver's numerical schemes. In the following, we describe the process in more detail. This study serves as a proof of concept, as we assimilate the mean velocity profile from a single APG TBL case. Our longer-term goal is to apply the approach to a larger set of DNS cases, on the order of $\mathcal{O}(10)$ – $\mathcal{O}(100)$.

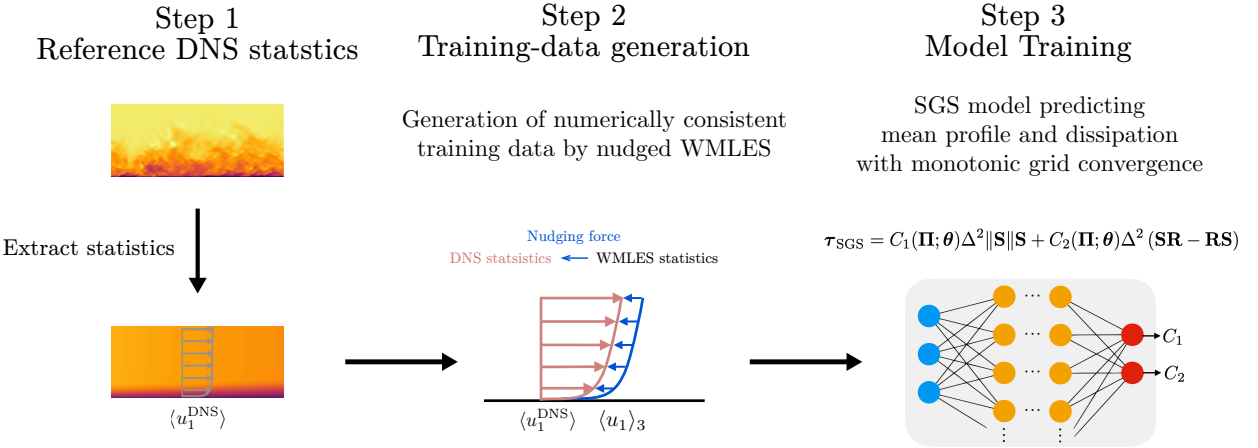


Figure 1: The three main steps for constructing the numerically consistent BFM SGS model.

2.1 DNS of an APG TBL

We train and test our model on a TBL case with moderate APG. The schematic of the simulation is shown in Figure 2. The adverse pressure gradient is introduced by prescribing a ceiling with a virtual straight ramp that deflects the freestream upward. The case considered in this study features a ramp angle $\alpha = 5^\circ$, and inflow momentum thickness Reynolds number $Re_\theta = U_\infty \theta / \nu = 670$.

The computational domain spans $L_x = 1200\theta_{in}$, $L_y = 200\theta_{in}$, and $L_z = 200\theta_{in}$ in the streamwise, wall-normal, and spanwise directions, respectively, where θ_{in} represents the momentum thickness at the inlet. The inflow conditions are generated by prescribing a mean velocity profile from a zero-pressure-gradient TBL at a matching Reynolds number (Sillero et al., 2013). Velocity fluctuations, extracted from a downstream recycling station, are superimposed on the mean profile located at $x_{\text{recycle}} = 100\theta_{in}$ using quasi-periodic conditions.

At the domain exit, a convective outlet boundary condition is implemented as $\partial \mathbf{u} / \partial t + U_\infty \partial \mathbf{u} / \partial x = \mathbf{0}$ (Pauley et al., 1990), modified by small corrections to ensure global mass conservation (Simens et al., 2009). The spanwise direction is treated as periodic, while the top boundary utilizes an inviscid potential-flow solution. This approach assumes a virtual wall located above the domain, modeled via a pure potential source. The wall-normal velocity at the upper boundary is defined as:

$$v|_{L_y} = \frac{U_\infty L_y [(x_{\text{ramp}} - x_{\text{source}})^2 + L_y^2]}{(x_{\text{ramp}} - x_{\text{source}}) [(x - x_{\text{source}})^2 + L_y^2]}, \quad (1)$$

where the source location x_{source} is derived by requiring the potential flow to be parallel to the linear ramp at x_{ramp} . This location represents the intersection of the ramp line with the horizontal wall:

$$x_{\text{source}} = x_{\text{ramp}} - Y_{\text{ramp}} \tan(\alpha). \quad (2)$$

To maintain irrotational flow at the top boundary, the streamwise velocity is determined by enforcing zero spanwise vorticity:

$$\omega_z|_{L_y} = \frac{\partial v|_{L_y}}{\partial x} - \frac{\partial u|_{L_y}}{\partial y} = 0. \quad (3)$$

Additionally, the spanwise velocity shear $\partial w / \partial y$ is set to zero at this boundary.

The incompressible Navier-Stokes equations are solved using DNS. Spatial derivatives are approximated using a second-order central finite difference scheme on a staggered grid (Orlandi, 2000). For temporal integration, a third-order Runge-Kutta scheme (Wray, 1990) is employed in conjunction with a fractional-step method (Kim and Moin, 1985). The solver has been validated in prior investigations of turbulent channel flows (Bae et al., 2018; Lozano-Durán et al., 2020), zero-pressure-gradient turbulent boundary layers (Towne et al., 2023), and transitional boundary layers (Lozano-Durán et al., 2018).

Some properties of the APG TBL are shown in Figure 3. The Clauser pressure-gradient parameter, $\beta = (\delta^* / \tau_w) dP/dx$, ranges from 0 to 2.8, where δ^* is the displacement thickness, τ_w is the wall-shear stress, and dP/dx is the streamwise freestream pressure gradient. The momentum-thickness Reynolds number increases from 500 at the inlet to 5,500 near the outlet.

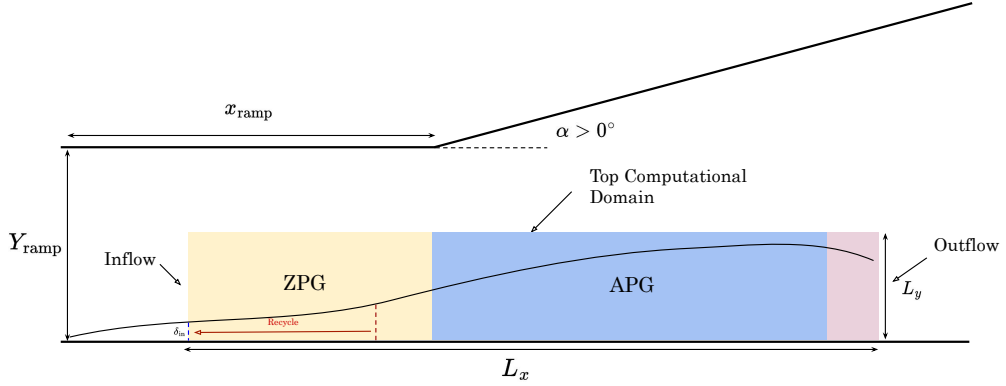
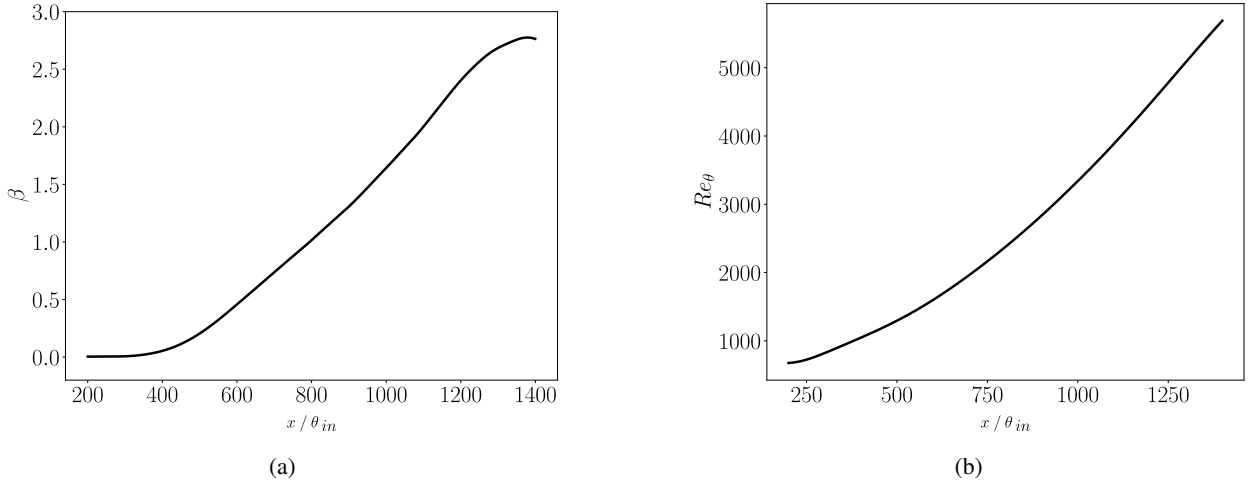


Figure 2: Schematic of the DNS setup of the APG TBL.

Figure 3: Some properties of the APG TBL computed by DNS are used for training and testing. (a) Clauser parameter β . (b) Momentum-thickness Reynolds number Re_θ .

2.2 Training data generation via nudging

The fundamental principle of nudging for a dynamical system is illustrated in Figure 4. Mathematically, this entails adding a relaxation term to the governing equations that nudges the instantaneous flow state toward an observed reference state, which is treated as the truth. Note, however, that this approach may not be well suited for practical WMLES for several reasons. First, the notion of a “true trajectory” is not well defined, since different coarse-graining procedures applied to DNS would generally yield different reference trajectories. Moreover, WMLES is chaotic, and forcing the instantaneous trajectory to closely track a reference trajectory is typically not possible without highly intrusive forcing. Finally, even if WMLES is successfully nudged to a reference trajectory, no SGS model can, in general, reproduce the required forcing without error, owing to the fundamental information loss inherent to coarse-grained systems (Lozano-Durán and Arranz, 2022). Because information from the small scales is irretrievably lost, there is, in general, no solution with negligible error.

In the present work, rather than assimilating the full coarse-grained trajectory, we assimilate only selected flow statistics. This offers several advantages: the target is well defined; the statistics are typically the quantities of practical interest; an SGS model that matches these statistical constraints can, in general, be discovered; and no costly space–time DNS data are required beyond the statistics, which may also be obtained from experiments. The statistical variant of nudging is achieved by adding a corrective term to the right hand side of the LES momentum equations:

$$\frac{\delta \mathbf{u}}{\delta t} + \mathbf{u} \cdot \nabla \mathbf{u} = -\frac{1}{\rho} \nabla p + \nabla \cdot (2\nu \mathbf{S}) + \nabla \cdot \boldsymbol{\tau}_{SGS}^{\text{base}} + \mathbf{F}_{\text{nudging}}, \quad (4)$$

where \mathbf{u} is the resolved (LES) velocity field, $\delta/\delta t$ denotes the discrete time marching of the solver, ∇ is the discrete nabla operator, ν is the kinematic viscosity, $\boldsymbol{\tau}_{SGS}^{\text{base}}$ is the baseline SGS stress tensor, \mathbf{S} is the resolved rate-of-strain tensor

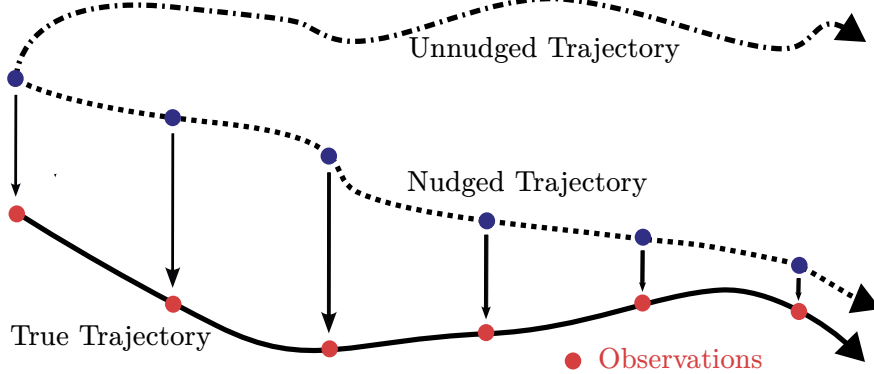


Figure 4: Schematic of nudging. Compared to the unnudged trajectory, nudging pushes the system to better match the true trajectory. The red circles are observations that are assumed to be the truth. Adapted from Asch et al. (2016).

Points per BL thickness	Coarse	Medium	Fine
Mean value	14	20	25
Range interval	[8, 24]	[10, 29]	[12, 36]

Table 1: Statistics for the number of grid points across the boundary layer thickness for three grid resolutions.

and $\mathbf{F}_{\text{nudging}}$ is the correction term representing nudging, which is adjusted based on the statistics to be assimilated. We define

$$\mathbf{F}_{\text{target}} = \nabla \cdot \boldsymbol{\tau}_{\text{SGS}}^{\text{base}} + \mathbf{F}_{\text{nudging}} \quad (5)$$

as the forcing term our SGS model aims to approach to predict the target statistics. The DSM is used as the baseline SGS closure during the training data generation, although other options are also possible. The selection of the DSM is motivated by previous reports of its robust performance in complex cases (Goc et al., 2021a, 2024).

In our previous work (Ling and Lozano-Duran, 2025), we showed how the nudging works for a channel-like simulation with only one inhomogeneous direction. To apply the approach to a TBL simulation with two inhomogeneous directions, we have

$$\mathbf{F}_{\text{nudging}} = -\alpha_n (\langle u_1 \rangle_3 - \langle u_1^{\text{DNS}} \rangle) \delta_{11}, \quad (6)$$

where $\mathbf{u} = [u_1, u_2, u_3]$, with indices 1, 2, and 3 denoting the streamwise, wall-normal, and spanwise directions, respectively, in a Cartesian coordinate system; δ_{ij} is the Kronecker delta; the operator $\langle \cdot \rangle_3$ denotes an average over the spanwise direction; α_n is a scalar that sets the strength of the nudging forcing set to the minimum value such that the relative error in the nudged mean velocity profile is below 1%; and $\langle u_1^{\text{DNS}} \rangle$ is the DNS streamwise mean velocity (averaged over the homogeneous directions and time).

We generate the training data for $\mathbf{F}_{\text{target}}$ using the nudging formulation above implemented in the same WMLES solver that is later used for *a posteriori* simulations. This guarantees consistency with the numerical discretization of the flow solver. In our prior work (Ling and Lozano-Duran, 2025), we employed a finite-difference code. Here, we implement the full training and testing workflow within the GPU-accelerated solver charLES (Cadence, Inc.). Our motivation for selecting this solver is to enable the application of the SGS model to cases with arbitrary geometric complexity. The charLES code is a compressible, second-order-accurate finite-volume solver that employs low-dissipation spatial discretization schemes. The solver leverages a Voronoi-diagram-based meshing strategy to generate high-quality unstructured grids and has been extensively validated across a broad range of flow configurations (Bres et al., 2017; Goc et al., 2021a, 2024, 2025).

Another important aspect of training data generation involves using a pre-trained wall model throughout the nudging phase. This ensures that the resulting flow fields incorporate the specific boundary-condition effects associated with that wall model, allowing the nudging force, and hence the SGS model, to learn wall-model-induced behaviour (Ling et al., 2022; Arranz et al., 2024). Here, we use the ML-based wall model BFM-WM-v2 developed by Ling et al. (2025) for both data generation and *a posteriori* testing. We select this wall model because it exhibits low internal error (i.e., the error induced when a wall model is provided with the correct outer-flow inputs).

Training data are generated for the nudged APG TBL at three grid resolutions, as summarized in Table 1. This setup allows the model to learn how to adjust its output across different grid resolutions and to enforce monotonic grid convergence. An instantaneous plot of the normalized streamwise velocity on the coarsest grid is shown in Figure 5.

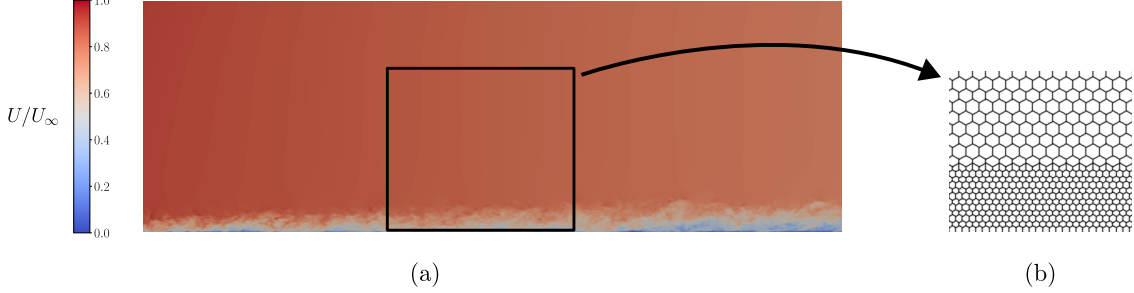


Figure 5: (a) The contour plot of the normalized instantaneous streamwise velocity at the center plane of the computational domain for the data generation of APG TBL case with a coarse grid. (b) The Voronoi grid in the black rectangular region shown in the left plot.

In summary, the nudged WMLES is performed using the `charLES` solver for the APG TBL configuration. This setup uses the wall model BFM-WM-v2, which is characterized by low internal error, together with the DSM baseline SGS closure, to produce numerically consistent datasets for training purposes. Finally, training data is generated for three grid resolutions.

2.3 SGS model formulation

We adopt a non-Boussinesq tensorial formulation for the SGS model, consistent with recent studies reporting improved performance (Lozano-Durán and Arranz, 2022; Agrawal et al., 2022; Zhou and Bae, 2024, 2025). The original expansion for the SGS stress tensor proposed by Lund (1992) contains five distinct terms. Here, we seek a balance between simplicity and accuracy by retaining a second term that accounts for the rotation tensor, \mathbf{R} . The resulting model reads

$$\tau_{\text{SGS}} = C_1(\boldsymbol{\Pi}; \boldsymbol{\theta}) \Delta^2 \|\mathbf{S}\| \mathbf{S} + C_2(\boldsymbol{\Pi}; \boldsymbol{\theta}) \Delta^2 (\mathbf{S} \mathbf{R} - \mathbf{R} \mathbf{S}), \quad (7)$$

where Δ is the characteristic grid size of a given control volume, and C_1 and C_2 are parameterized by a dual-output artificial neural network (ANN) with parameters $\boldsymbol{\theta}$. The ANN takes as inputs the variables $\boldsymbol{\Pi}$, which are dimensionless to ensure that the model is invariant under changes of units. For the ANNs, we employ a multi-layer perceptron architecture consisting of four hidden layers, each with twenty neurons. The rectified linear unit is utilized as the activation function for all hidden layers. The dimensionless inputs $\boldsymbol{\Pi}$ are constructed from the dimensional variables:

$$\mathbf{Q} = \{I_1, I_2, I_3, I_4, I_5, \nu, \Delta\}, \quad (8)$$

where I_i , $i = 1, \dots, 5$, are local invariants of \mathbf{S} and \mathbf{R} (Lund, 1992):

$$\begin{aligned} I_1 &= \text{tr}(\mathbf{S}^2), & I_2 &= \text{tr}(\mathbf{R}^2), \\ I_3 &= \text{tr}(\mathbf{S}^3), & I_4 &= \text{tr}(\mathbf{S} \mathbf{R}^2), \\ I_5 &= \text{tr}(\mathbf{S}^2 \mathbf{R}^2). \end{aligned} \quad (9)$$

The use of these invariants to construct $\boldsymbol{\Pi}$ ensures that the model is equivariant under translations and rotations, and invariant under Galilean transformations.

To determine the optimal dimensionless inputs, we use the information-theoretic Buckingham- π theorem from Yuan and Lozano-Durán (2025). This approach leverages information-theoretic principles to identify the input variables that maximize the predictive power of the output regardless of the model structure (from analytical functions to neural networks). The core premise is that the performance of a model is fundamentally bounded by the information shared between inputs and outputs (Lozano-Durán and Arranz, 2022), defined formally by Shannon information (Shannon, 1948).

Since explicit target values for C_1 and C_2 are unavailable, in contrast to standard supervised learning, we cannot directly measure the mutual information of $\boldsymbol{\Pi}$ with respect to these coefficients. Instead, we optimize a lower-bound proxy to select the optimal inputs. Since predicting the target forcing remains the primary goal, this selection is based on the relationship between the dimensionless mean forcing and the mean inputs. Consider the functional dependency chain:

$$C_1, C_2 \rightarrow \mathbf{F}_{\text{target}} \rightarrow \langle \mathbf{F}_{\text{target}} \rangle, \quad (10)$$

where each arrow represents a deterministic mathematical operation. The data-processing inequality (Cover, 1999) states that such operations cannot increase mutual information. Consequently, we have the following relationships:

$$I(\langle \boldsymbol{\Pi} \rangle; \langle \mathbf{F}_{\text{target}} \rangle) \leq I(\boldsymbol{\Pi}; \langle \mathbf{F}_{\text{target}} \rangle) \leq I(\boldsymbol{\Pi}; \mathbf{F}_{\text{target}}) \leq I(\boldsymbol{\Pi}; C_1, C_2), \quad (11)$$

where $I(\cdot; \cdot)$ denotes the mutual information. While the information-theoretic Buckingham- π theorem implies that $I(\boldsymbol{\Pi}; C_1, C_2)$ is the target quantity for optimization, data availability restricts us to computing the leftmost term, $I(\langle \boldsymbol{\Pi} \rangle; \langle \mathbf{F}_{\text{target}} \rangle)$. Therefore, by maximizing this term, we effectively optimize a lower bound on $I(\boldsymbol{\Pi}; C_1, C_2)$. Applying this procedure yields the following set of optimal dimensionless inputs:

$$\boldsymbol{\Pi} = \left[\frac{I_1^{1/2} \Delta^2}{\nu}, \quad \frac{I_3}{I_1^{3/2}}, \quad \frac{I_5}{I_1^2}, \quad \frac{I_4}{I_1^{3/2}}, \quad \frac{I_3 I_4}{I_1^3} \right]. \quad (12)$$

2.4 Loss function and training details

The loss function has two components: one to promote accurate prediction of $\langle \mathbf{F}_{\text{target},i} \rangle_3$ and another to match the dissipation of the baseline and learned SGS models. The problem is formulated using a multiple-instance learning approach analogous to Ling and Lozano-Duran (2025). Samples at each grid resolution are partitioned into $K = 3$ datasets, such that the i -th dataset contains N_i samples. The first component of the loss for the i -th dataset, which targets the nudging forcing, is defined as

$$\mathcal{L}_{\text{forcing},i} = \frac{1}{N_i} \left\| \langle \mathbf{F}_{\text{pred}} \rangle_3 - \langle \mathbf{F}_{\text{target}} \rangle_3 \right\|^2, \quad (13)$$

$$\mathbf{F}_{\text{pred}} = \nabla \cdot \boldsymbol{\tau}_{\text{SGS}}, \quad (14)$$

where $\mathbf{F}_{\text{pred},i}$ is the forcing predicted by the learned model, and the subscript i denotes samples constrained to belong to the i -th dataset. Note that the target forcing $\mathbf{F}_{\text{target}}$ does not, in general, conserve momentum, since it may act as a source or sink. In contrast, the learned model $\boldsymbol{\tau}_{\text{SGS}}$ is momentum-conserving, because it enters the dynamics only through its divergence.

The second component of the loss function ensures that the model reproduces the dissipation induced by the SGS stresses. We first note that the second tensor-expansion term in Eq. 7 does not contribute to mean SGS dissipation or production, due to symmetry. A close inspection of the energy equation in Appendix A indicates that the nudging term should induce additional dissipation. However, order-of-magnitude arguments show that the dissipation associated with the nudging term is negligible compared with that of the eddy-viscosity term (Appendix B). We therefore neglect the nudging contribution and define the dissipation loss for the i -th dataset as

$$\mathcal{L}_{\text{dissipation},i} = \frac{1}{N_i} \left\| \langle \varepsilon_{\text{pred}} \rangle_3 - \langle \varepsilon_{\text{target}} \rangle_3 \right\|^2, \quad (15)$$

$$\varepsilon_{\text{pred}} = \boldsymbol{\tau}_{\text{SGS}} : \mathbf{S}, \quad (16)$$

$$\varepsilon_{\text{target}} = \boldsymbol{\tau}_{\text{SGS}}^{\text{base}} : \mathbf{S}, \quad (17)$$

where $:$ denotes the inner product. The final loss function is

$$\mathcal{L}_{\text{total}} = \sum_{i=1}^{K=3} w_i (\beta_{d,i} \mathcal{L}_{\text{dissipation},i} + \beta_{f,i} \mathcal{L}_{\text{forcing},i}), \quad (18)$$

where weights w_i provides a mechanism to adjust the contribution of each dataset based on its perceived importance and $\beta_{d,i}$ and $\beta_{f,i}$ are weights adjusted dynamically to ensure that the loss components are dimensionally consistent and comparable in magnitude. Specifically, these are defined as the inverse of the running mean of their respective loss components, $\beta_{k,i} = 1/\mu_{k,i}$ for $k \in \{d, f\}$ and $i \in \{1, 2, 3\}$. At each training epoch m , the running mean $\mu_{k,i}$ is updated via an exponential moving average as follows:

$$\mu_{k,i}^{(m)} = (1 - \gamma) \mu_{k,i}^{(m-1)} + \gamma \mathcal{L}_{k,i}^{(m)}, \quad (19)$$

where $\gamma \in (0, 1]$ is a smoothing momentum hyperparameter, set to be 0.9 in this work.

Regarding the weights w_i , we consider two cases: (i) equal weights across datasets, and (ii) resolution-dependent weights. The latter aims to assess whether emphasizing finer-grid datasets improves convergence under grid refinement, rather than assigning the same importance to lower-resolution cases. The weights used in each case are summarized in Table 2.

For each dataset, 30,000 individual streamwise stations are included, with the individual station serving as the fundamental unit for data splitting and sampling. The total dataset is partitioned into training, validation, and testing subsets using a 7:1.5:1.5 ratio. The model is implemented using PyTorch (Paszke et al., 2019) and optimized via the Adam algorithm (Kingma and Ba, 2017) with an initial learning rate of 0.0005 and decay rates of 0.9 and 0.999. To ensure robust convergence, the learning rate is reduced by a factor of 0.975 if the validation loss fails to decrease for 5 consecutive epochs. Furthermore, an early stopping criterion terminates the training process if no improvement is observed for 20 epochs.

	w_{Coarse}	w_{Medium}	w_{Fine}
Unequal Weights	1	10	100
Equal Weights	1	1	1

Table 2: Two versions of the model with different weight configurations assigned to datasets at each resolution.

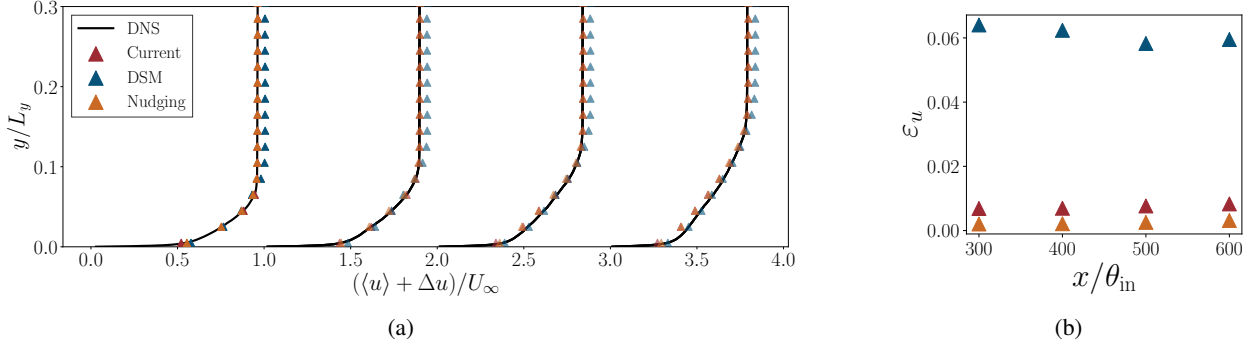


Figure 6: *A posteriori* testing of the current SGS model and the DSM both with BFM-WM-v2 in WMLES of an APG TBL. The configuration corresponds to a turbulent boundary layer developing under a top ramp inclined at 5°. (a) Mean velocity profiles at four streamwise locations, $x/L_y = 3, 4, 5$, and 6 ($x/\theta_{\text{in}} = 300, 400, 500, 600$) as a function of the wall normal direction y . Profiles are vertically shifted by $\Delta u/U_\infty = x/L_y - 3$ for clarity. (b) Integrated relative error ε_u at these stations.

3 Results

3.1 A posteriori test at the finest grid size

We present *a posteriori* results for the highest grid resolution used during training (the fine grid in Table 1), using the DSM with the same wall model BFM-WM-v2 as the benchmark. Results obtained with other grid resolutions were found to be qualitatively similar.

The predicted mean streamwise velocity profiles (here denoted by u for simplicity) at selected streamwise locations are presented in Figure 6a. To quantify the predictive accuracy across the domain, we compute the integrated error, ε_u , defined as

$$\varepsilon_u = \frac{1}{\delta} \int_0^\delta \frac{|\langle u \rangle - \langle u^{\text{DNS}} \rangle|}{U_e} dy, \quad (20)$$

where δ denotes the boundary-layer thickness and U_e is the edge velocity. As shown in Figure 6b, the current SGS model significantly outperforms the standard DSM and yields results comparable to the optimal nudged prediction.

Figure 7 illustrates the prediction of the skin-friction coefficient. As anticipated, the discrepancies in the mean velocity profile produced by the DSM translate into substantial errors in the wall-shear stress. Conversely, the current SGS model closely tracks the reference data. In certain regions, the current model appears to outperform even the nudged simulation, i.e., the theoretical ideal forcing. This counterintuitive result is likely attributable to partial error cancellation between the SGS model and the wall model, creating an illusion of superior performance compared to the nudged flow.

3.2 Convergence behavior with grid refinement

The convergence behavior of the model is analyzed in Figure 8. We adopt the integrated error in the mean velocity, $\bar{\varepsilon}_u$, as the primary metric for assessing convergence. The reported error is averaged over the region of interest $x/\theta_{\text{in}} \in [300, 700]$.

Results are shown for the three grid resolutions used in training. We first consider the trained SGS model with equal weights across the three grid sizes. For this unweighted model, the coarsest grid paradoxically yields the smallest error, while the error increases at finer resolutions. This is a trend contrary to the desired monotonic grid-convergence behavior. By contrast, employing the proposed weighting strategy recovers a consistent convergence trend. Although the finest resolution remains under-resolved and not yet fully converged, the multi-task strategy of assigning distinct weights to different grid resolutions clearly promotes the monotonic grid convergence desired in WMLES.

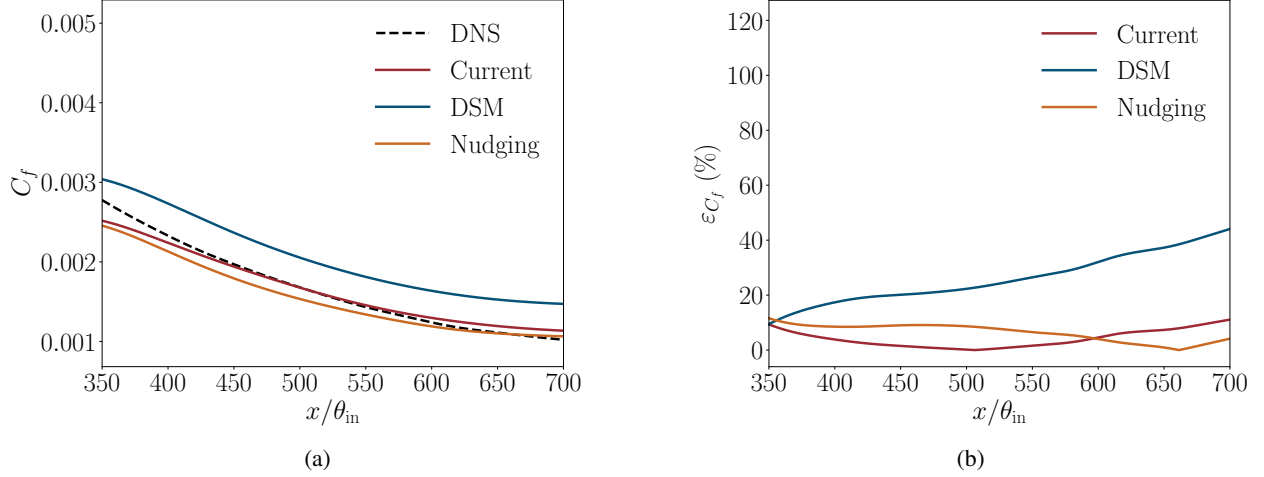


Figure 7: (a) Streamwise distribution of the predicted skin-friction coefficient C_f by the current SGS model and the DSM both with BFM-WM-v2 in WMLES of an APG TBL. (b) Relative error $\varepsilon_{C_f} = (C_{f,\text{pred}} - C_{f,\text{DNS}})/C_{f,\text{DNS}}$.

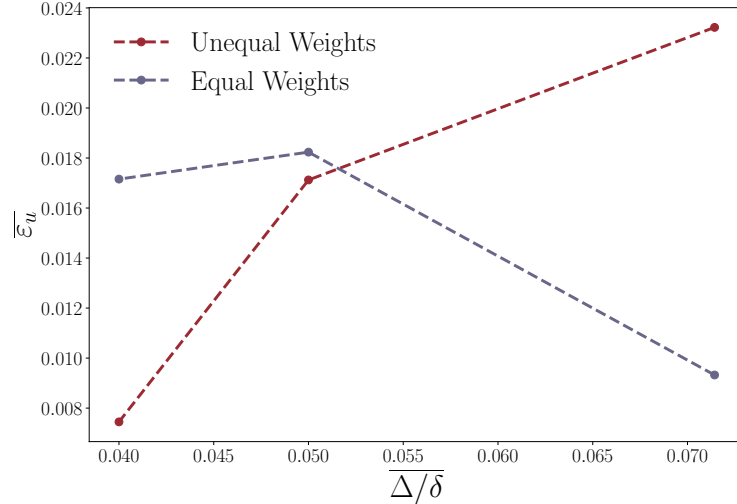


Figure 8: Comparison of mean velocity error at different grid resolutions using SGS models trained with equal weights and unequal weights.

4 Discussion

4.1 General nudging scheme

The current nudging-based data assimilation approach constructs a one-dimensional forcing term for the streamwise velocity. While effective for canonical boundary layers and channels at moderate mean pressure gradients, this formulation restricts the applicability of the method to flows whose mean statistical state varies strongly in more than one direction, such as separated flows. Other examples include square-duct configurations or wing–body junctions, where secondary mean motions are critical (Pirozzoli et al., 2018). In such cases, the nudging force becomes vector-valued, correcting not only the streamwise momentum deficit but also driving the secondary cross-stream vortices (the v and w components) that are often under-resolved in standard WMLES. It remains to be shown whether this straightforward extension is robust for these more complex configurations.

Furthermore, the scope of assimilation can be expanded beyond first-order moments (mean velocity) to include higher-order turbulence statistics, such as resolved Reynolds stresses or the turbulent kinetic energy dissipation rate. Assimilating dissipation is particularly attractive for training SGS models, as it directly constrains the energy transfer from resolved to subgrid scales. However, this introduces a coupled optimization challenge: forcing terms designed

to correct second-order statistics must be introduced without contaminating the mean-flow forcing. It is not yet clear whether this extension can be implemented without degrading the original performance.

4.2 SGS model tensor form

The current model formulation incorporates two terms from the complete five-term integrity basis derived by Lund (1992). This parsimonious choice was made to enhance specific structural properties without directly altering the SGS dissipation characteristics. However, for flow regimes exhibiting more complex stress anisotropies—such as corner flows, junctions, or systems with strong rotation—the remaining terms in the expansion may become necessary. Arbitrarily including all five terms, however, increases both computational cost and the risk of overfitting the training data. To address this, future work will explore principled feature-selection techniques to identify an optimal subset of tensor terms.

4.3 Scalability via automated multi-task learning

The current work establishes a proof of concept for using resolution-dependent loss weighting to enforce grid convergence in data-driven SGS models. However, this demonstration was limited to a single flow configuration with a manually tuned weighting schedule. To ensure the method is robust enough for general-purpose deployment, future work must assess its performance across a broader training database, such as the diverse collection of APG TBL cases with varying Reynolds numbers and pressure-gradient histories presented by Ling et al. (2025).

Scaling this approach to multiple flow cases exposes a critical limitation of the current strategy: reliance on fixed, manually assigned weights. As the number of training cases and grid levels increases, the hyperparameter space for these weights becomes prohibitively large to tune by hand. Consequently, integrating automated multi-task learning algorithms becomes essential.

Promising approaches exist, such as the Pareto-optimal training strategy for turbulence modeling demonstrated by Liu et al. (2025), or the homoscedastic uncertainty weighting proposed by Kendall et al. (2018), which dynamically balances loss terms based on intrinsic task uncertainty. However, applying these methods directly to WMLES presents a unique challenge. Standard algorithms typically aim to balance performance across all tasks or focus on “easy” tasks first. In contrast, our physical constraint is hierarchical: error reduction on finer grids must be prioritized over coarser grids to satisfy consistency requirements. Determining how to modify existing automated objectives to strictly enforce this specific convergence hierarchy, rather than merely balancing errors, remains an open and nontrivial question for future research.

5 Conclusions

This study presents a data-driven, numerically consistent SGS model for WMLES. The model is constructed using a statistical formulation of nudging, which is applied to a turbulent boundary layer under an adverse pressure gradient. The results demonstrate the robustness of this data-assimilation-based training strategy for flows with increased complexity.

In addition to statistical nudging, we introduced two primary modifications to our previous data-driven SGS modeling approach to improve performance and numerical convergence. First, we adopted a non-Boussinesq tensorial formulation and added a dissipation constraint to the loss function. The resulting model outperforms the standard dynamic Smagorinsky model coupled with the same wall model for the case examined. Second, we developed a multi-task learning method to control the convergence behavior of the data-driven SGS model. By weighting the training datasets according to grid resolution, we enforce consistent error reduction with grid refinement. This strategy helps address a persistent challenge in WMLES, where interaction errors among wall models, numerics, and SGS models often produce non-monotonic convergence.

Acknowledgement

This work was supported by the National Science Foundation (NSF) under grant number #2317254 and NSF CAREER #2140775. The project is also supported by an Early Career Faculty grant from NASA’s Space Technology Research Grants Program (grant #80NSSC23K1498). The authors acknowledge the MIT Office of Research Computing and Data for providing high performance computing resources that have contributed to the research results reported within this paper. This work also used the DeltaAI and Delta system at the National Center for Supercomputing Applications: Services and Support (ACCESS) program, which is supported by National Science Foundation grants #2138259, #2138286, #2138307, #2137603, and #2138296.

A SGS energy equation for streamwise nudged WMLES governing equations

Suppose that we are only nudging in the streamwise direction and we set it in the x direction. Then the SGS energy equation is

$$\frac{\partial k_{sgs}}{\partial t} + \bar{u}_j \frac{\partial k_{sgs}}{\partial x_j} = - \underbrace{\tau_{ij} \bar{S}_{ij}}_{\text{SGS production } \varepsilon_{sgs}} - \underbrace{\alpha \overline{(u_1 - \bar{u}_1) F_1}}_{\text{Nudging production } S_{k_{sgs}}} + \nu \frac{\partial^2 k_{sgs}}{\partial x_j \partial x_j} - \frac{\partial}{\partial x_j} \left(\frac{1}{2} \overline{u'_i u'_i u'_j} + \frac{1}{\rho} \overline{p' u'_j} \right) - \nu \overline{\frac{\partial u'_i}{\partial x_j} \frac{\partial u'_i}{\partial x_j}}, \quad (21)$$

where the first two terms correspond to the production of SGS energy production from the SGS term (ε_{sgs}) and nudging term ($S_{k_{sgs}}$) and therefore the dissipation from the resolved energy. $F_1 = \alpha(\langle u_1 \rangle_3 - \langle u_1^{\text{DNS}} \rangle)$ is the magnitude of F_{nudging} in Eq. 6.

B Order-of-Magnitude analysis of the resolved energy dissipation: SGS vs. Nudging

We compare the magnitudes of $|\varepsilon_{sgs}|$ and $|S_{k_{sgs}}|$ in a typical WMLES with high Reynolds number. First, if ε_{sgs} is only a function of k_{sgs} and Δ , we assume $\varepsilon_{sgs} = C_\varepsilon k_{sgs}^{3/2}/\Delta$ and the scaling $k_{sgs} \sim (u'_{sgs})^2$ holds. Then we have

$$|\varepsilon_{sgs}| \sim \frac{(u'_{sgs})^3}{\Delta}. \quad (22)$$

Then for the Nudging term, we assume that the relevant velocity scale is outer scale U and outer length scale L . Mark the SGS fluctuation $u_1 - \bar{u}_1 = \tilde{u}_1$. Then we have the magnitude $|S_{k_{sgs}}| \sim |\tilde{u}_1| \cdot |F_1| \cdot \rho_{\tilde{u}_1 F_1}$, where $\rho_{\tilde{u}_1 F_1}$ is the correlation coefficient. Since the SGS fluctuation scales with the deviation from the mean, $|\tilde{u}_1| \sim u'_{sgs}$, and $F_1 \sim U^2/L$ by dimensional analysis, we have

$$|S_{k_{sgs}}| \sim u'_{sgs} \cdot \frac{U^2}{L} \cdot \rho_{\tilde{u}_1 F_1}. \quad (23)$$

Then we calculate the ratio between two terms:

$$\frac{|\varepsilon_{sgs}|}{|S_{k_{sgs}}|} \sim \frac{(u'_{sgs})^3/\Delta}{u'_{sgs} \cdot (U^2/L) \cdot \rho_{\tilde{u}_1 F_1}} = \left(\frac{u'_{sgs}}{U} \right)^2 \cdot \frac{L}{\Delta} \cdot \frac{1}{\rho_{\tilde{u}_1 F_1}}. \quad (24)$$

By assuming that the flow is in inertial subrange and therefore equating the dissipation from the outer large scale and inner scale, we have $(u'_{sgs}/U) \sim (\Delta/L)^{1/3}$. Using this scaling leads to

$$\frac{|\varepsilon_{sgs}|}{|S_{k_{sgs}}|} \sim \left(\left(\frac{\Delta}{L} \right)^{1/3} \right)^2 \cdot \frac{L}{\Delta} \cdot \frac{1}{\rho_{\tilde{u}_1 F_1}} = \left(\frac{\Delta}{L} \right)^{2/3} \cdot \frac{L}{\Delta} \cdot \frac{1}{\rho_{\tilde{u}_1 F_1}} = \left(\frac{L}{\Delta} \right)^{1/3} \cdot \frac{1}{\rho_{\tilde{u}_1 F_1}}. \quad (25)$$

By scale separation assumption, we have $\Delta \ll L$ and the correlation between \tilde{u}_1 (decided by the small scale) and F_1 (decided by the large scale) is small. Therefore, it is reasonable to assume $\rho_{\tilde{u}_1 F_1} \ll 1$. Putting all these together, we conclude that for a typical WMLES at high Reynolds number, we have

$$|\varepsilon_{sgs}| \gg |S_{k_{sgs}}|.$$

References

Rahul Agrawal, Michael P. Whitmore, Kevin P. Griffin, Sanjeeb T. Bose, and Parviz Moin. Non-Boussinesq subgrid-scale model with dynamic tensorial coefficients. *Phys. Rev. Fluids*, 7(7):074602, July 2022. ISSN 2469-990X. doi: 10.1103/PhysRevFluids.7.074602.

Gonzalo Arranz, Yuenong Ling, Sam Costa, Konrad Goc, and Adrián Lozano-Durán. Building-block-flow computational model for large-eddy simulation of external aerodynamic applications. *Commun. Eng.*, 3(1):127, September 2024. ISSN 2731-3395. doi: 10.1038/s44172-024-00278-1.

Mark Asch, Marc Bocquet, and Maëlle Nodet. *Data Assimilation: Methods, Algorithms, and Applications*. Number 11 in Fundamentals of Algorithms. Society for Industrial and Applied Mathematics, Philadelphia, 2016. ISBN 978-1-61197-454-6.

H Jane Bae and Adrian Lozano-Duran. Numerical and modeling error assessment of large-eddy simulation using direct-numerical-simulation-aided large-eddy simulation. *arXiv preprint arXiv:2208.02354*, 2022.

HJ Bae and A Lozano-Durán. Towards exact subgrid-scale models for explicitly filtered large-eddy simulation of wall-bounded flows. *Annual research briefs. Center for Turbulence Research (US)*, 2017:207, 2017.

HJ Bae and A Lozano-Durán. Dns-aided explicitly filtered les of channel flow. *Annual research briefs. Center for Turbulence Research (US)*, 2018:197, 2018.

Hyunji Jane Bae, Adrián Lozano-Durán, ST Bose, and Parviz Moin. Turbulence intensities in large-eddy simulation of wall-bounded flows. *Phys. Rev. Fluids*, 3(1):014610, 2018.

Andrea Beck and Marius Kurz. Toward Discretization-Consistent Closure Schemes for Large Eddy Simulation Using Reinforcement Learning. *Phys. Fluids*, 35(12):125122, December 2023. ISSN 1070-6631, 1089-7666. doi: 10.1063/5.0176223.

Sanjeeb T. Bose and George Ilhwan Park. Wall-Modeled Large-Eddy Simulation for Complex Turbulent Flows. *Annu. Rev. Fluid Mech.*, 50(1):535–561, 2018. doi: 10.1146/annurev-fluid-122316-045241.

Guillaume A Bres, Frank E Ham, Joseph W Nichols, and Sanjiva K Lele. Unstructured large-eddy simulations of supersonic jets. *AIAA J.*, 55(4):1164–1184, 2017.

Haecheon Choi, Chonghyuk Cho, Myunghwa Kim, and Jonghwan Park. Perspective on machine-learning-based large-eddy simulation. *Physical Review Fluids*, 10(11):110701, 2025. doi: 10.1103/bxen-rmdv.

Thomas M Cover. *Elements of information theory*. John Wiley & Sons, 1999.

Karthik Duraisamy. Perspectives on machine learning-augmented reynolds-averaged and large eddy simulation models of turbulence. *Physical Review Fluids*, 6(5):050504, 2021. doi: 10.1103/PhysRevFluids.6.050504.

Sagy R. Ephrati. Probabilistic data-driven turbulence closure modeling by assimilating statistics. *J. Comput. Phys.*, 539: 114234, 2025. ISSN 0021-9991. doi: 10.1016/j.jcp.2025.114234.

Sagy R Ephrati, Arnout Franken, Erwin Luesink, Paolo Cifani, and Bernard J Geurts. Continuous data assimilation closure for modeling statistically steady turbulence in large-eddy simulation. *Phys. Rev. Fluids*, 10(1):013801, 2025.

Xiantao Fan, Xin-Yang Liu, Meng Wang, and Jian-Xun Wang. Diff-flowfsi: A gpu-optimized differentiable cfd platform for high-fidelity turbulence and fsi simulations. *Comput. Methods Appl. Mech. Eng.*, 448:118455, 2026.

Masataka Gamahara and Yuji Hattori. Searching for turbulence models by artificial neural network. *Phys. Rev. Fluids*, 2(5):054604, May 2017. ISSN 2469-990X. doi: 10.1103/PhysRevFluids.2.054604.

Konrad A. Goc. *Towards Certification by Analysis: Large-Eddy Simulations of Commercial Aircraft Across the Flight Envelope*. PhD thesis, Leland Stanford Junior University, Stanford, CA, March 2023.

Konrad A Goc, Oriol Lehmkuhl, George Ilhwan Park, Sanjeeb T Bose, and Parviz Moin. Large eddy simulation of aircraft at affordable cost: a milestone in computational fluid dynamics. *Flow*, 1:E14, 2021a.

Konrad A Goc, Oriol Lehmkuhl, George Ilhwan Park, Sanjeeb T. Bose, and Parviz Moin. Large eddy simulation of aircraft at affordable cost: A milestone in computational fluid dynamics. *Flow*, 1:E14, 2021b. ISSN 2633-4259. doi: 10.1017/flo.2021.17.

Konrad A Goc, Parviz Moin, Sanjeeb T Bose, and Adam M Clark. Wind tunnel and grid resolution effects in large-eddy simulations of the high-lift common research model. *J. Aircr.*, 61(1):267–279, 2024.

Konrad A Goc, Rahul Agrawal, Sanjeeb T Bose, and Parviz Moin. Studies of transonic aircraft flows and prediction of initial buffet using large-eddy simulation. *J. Aircr.*, pages 1–21, 2025.

Imran Hayat and George Ilhwan Park. Wall-Modeled Large-Eddy Simulation of Turbulent Boundary Layer with Spatially Varying Pressure Gradients. *AIAA J.*, 62(2):557–572, February 2024. ISSN 0001-1452, 1533-385X. doi: 10.2514/1.J063336.

Rik Hoekstra and Wouter Edeling. Reduced subgrid scale terms in three-dimensional turbulence. *Comput. Methods in Appl. Mech. Eng.*, 449:118506, 2026.

Rik Hoekstra, Daan Crommelin, and Wouter Edeling. Reduced data-driven turbulence closure for capturing long-term statistics. *Comput. Fluids*, 285:106469, December 2024. ISSN 00457930. doi: 10.1016/j.compfluid.2024.106469.

Xiaohan Hu, Imran Hayat, and George Ilhwan Park. Wall-modelled large-eddy simulation of three-dimensional turbulent boundary layer in a bent square duct. *J. Fluid Mech.*, 960:A29, April 2023. ISSN 0022-1120, 1469-7645. doi: 10.1017/jfm.2023.143.

Xiaohan Hu, Xiang Yang, and George Ilhwan Park. On the grid convergence of wall-modeled large-eddy simulation. *J. Comput. Phys.*, 504:112884, 2024.

Xinyi Huang, Sze Chai Leung, and H Jane Bae. Consistency requirement of data-driven subgrid-scale modeling in large-eddy simulation. *arXiv preprint arXiv:2511.15775*, 2025.

Prahladh S Iyer and Mujeeb R Malik. Efficient dynamic mixed subgrid-scale model. *Phys. Rev. Fluids*, 9(9):L092601, 2024.

Javier Jimenez and Robert Moser. LES - Where are we and what can we expect. In *29th AIAA, Fluid Dynamics Conference*, pages 1–11, Albuquerque, NM, U.S.A., June 1998. American Institute of Aeronautics and Astronautics. doi: 10.2514/6.1998-2891.

Myeongseok Kang, Youngmin Jeon, and Donghyun You. Neural-network-based mixed subgrid-scale model for turbulent flow. *J. Fluid Mech.*, 962:A38, 2023.

Soshi Kawai and Johan Larsson. Wall-modeling in large eddy simulation: Length scales, grid resolution, and accuracy. *Phys. Fluids*, 24(1):015105, January 2012. ISSN 1070-6631, 1089-7666. doi: 10.1063/1.3678331.

Alex Kendall, Yarin Gal, and Roberto Cipolla. Multi-task learning using uncertainty to weigh losses for scene geometry and semantics. In *Proceedings of the IEEE conference on computer vision and pattern recognition*, pages 7482–7491, 2018.

John Kim and Parviz Moin. Application of a fractional-step method to incompressible navier-stokes equations. *J. Comput. Phys.*, 59(2):308–323, 1985.

Junhyuk Kim, Hyojin Kim, Jiyeon Kim, and Changhoon Lee. Deep reinforcement learning for large-eddy simulation modeling in wall-bounded turbulence. *Phys. Fluids*, 34(10), 2022.

Myunghwa Kim, Jonghwan Park, and Haecheon Choi. Large eddy simulation of flow over a circular cylinder with a neural-network-based subgrid-scale model. *J. Fluid Mech.*, 984:A6, 2024.

Diederik P. Kingma and Jimmy Ba. Adam: A method for stochastic optimization, 2017.

Marius Kurz, Andrea Beck, and Benjamin Sanderse. Harnessing equivariance: Modeling turbulence with graph neural networks. *arXiv preprint arXiv:2504.07741*, 2025.

Johan Larsson, Soshi Kawai, Julien Bodart, and Ivan Bermejo-Moreno. Large eddy simulation with modeled wall-stress: Recent progress and future directions. *Mech. Eng. Rev.*, 3(1):15–00418–15–00418, 2016. ISSN 2187-9753. doi: 10.1299/mer.15-00418.

Dong Li, Lei Yang, Kai Zhang, Kun Luo, and Jianren Fan. Mixed subfilter-scale models for large-eddy simulation of decaying isotropic turbulence using an artificial neural network. *Comput. Fluids*, 289:106557, 2025.

Yuenong Ling and Adrian Lozano-Duran. Numerically consistent data-driven subgrid-scale model via data assimilation and machine learning. In *AIAA SCITECH 2025 Forum*, page 1280, 2025.

Yuenong Ling, Gonzalo Arranz, Emily Williams, Konrad Goc, Kevin Griffin, and Adrián Lozano-Durán. Wall-modeled large-eddy simulation based on building-block flows. In *Proceedings of the 2022 Summer Program*, pages 5–24, Stanford, December 2022. Center for Turbulence Research. doi: 10.48550/arXiv.2212.05120.

Yuenong Ling, Imran Hayat, Konrad Goc, and Adrian Lozano-Duran. General-purpose data-driven wall model for low-speed flows part i: Baseline model. *arXiv preprint arXiv:2511.16511*, 2025.

Björn List, Li-Wei Chen, and Nils Thuerey. Learned turbulence modelling with differentiable fluid solvers: physics-based loss functions and optimisation horizons. *J. Fluid Mech.*, 949:A25, 2022.

Bo Liu, Huiyang Yu, Haibo Huang, Nansheng Liu, and Xiyun Lu. Investigation of nonlocal data-driven methods for subgrid-scale stress modeling in large eddy simulation. *AIP Adv.*, 12(6), 2022.

Zhuo-Ran Liu, Hao-Chen Wang, Zhuo-Lin Zhao, and Heng Xiao. Towards a unified turbulence model through multi-objective learning. *arXiv preprint arXiv:2509.17189*, 2025.

A. Lozano-Durán, M. J. P. Hack, and P. Moin. Modeling boundary-layer transition in direct and large-eddy simulations using parabolized stability equations. *Phys. Rev. Fluids*, 3:023901, Feb 2018.

Adrián Lozano-Durán and Gonzalo Arranz. Information-theoretic formulation of dynamical systems: Causality, modeling, and control. *Phys. Rev. Research*, 4(2):023195, June 2022. ISSN 2643-1564. doi: 10.1103/PhysRevResearch.4.023195.

Adrián Lozano-Durán and Gonzalo Arranz. Information-theoretic formulation of dynamical systems: Causality, modeling, and control. *Phys. Rev. Res.*, 4(2):023195, 2022.

Adrián Lozano-Durán and H. Jane Bae. Machine learning building-block-flow wall model for large-eddy simulation. *J. Fluid Mech.*, 963:A35, May 2023. ISSN 0022-1120, 1469-7645. doi: 10.1017/jfm.2023.331.

Adrián Lozano-Durán and Hyunji Jane Bae. Error scaling of large-eddy simulation in the outer region of wall-bounded turbulence. *J. Comput. Phys.*, 392:532–555, September 2019. ISSN 0021-9991. doi: 10.1016/j.jcp.2019.04.063.

Adrián Lozano-Durán, Marco G Giometto, George Ilhwan Park, and Parviz Moin. Non-equilibrium three-dimensional boundary layers at moderate reynolds numbers. *J. Fluid Mech.*, 883:A20, 2020.

Adrián Lozano-Durán, Sanjeeb T. Bose, and Parviz Moin. Performance of Wall-Modeled LES with Boundary-Layer-Conforming Grids for External Aerodynamics. *AIAA J.*, 60(2):747–766, February 2022. ISSN 0001-1452, 1533-385X. doi: 10.2514/1.J061041.

T. S. Lund. Parameterization of subgrid-scale stress by the velocity gradient tensor. In *Annual Research Briefs*, pages 27–43. Center for Turbulence Research, 1992.

TS Lund. The use of explicit filters in large eddy simulation. *Computers & Mathematics with Applications*, 46(4): 603–616, 2003.

Jonathan F. MacArt, Justin Sirignano, and Jonathan B. Freund. Embedded training of neural-network subgrid-scale turbulence models. *Phys. Rev. Fluids*, 6(5):050502, May 2021. ISSN 2469-990X. doi: 10.1103/PhysRevFluids.6.050502.

Mori Mani and Andrew J. Dorgan. A Perspective on the State of Aerospace Computational Fluid Dynamics Technology. *Annu. Rev. Fluid Mech.*, 55(1):431–457, January 2023. ISSN 0066-4189, 1545-4479. doi: 10.1146/annurev-fluid-120720-124800.

R. Maulik, O. San, A. Rasheed, and P. Vedula. Subgrid modelling for two-dimensional turbulence using neural networks. *J. Fluid Mech.*, 858:122–144, January 2019. ISSN 0022-1120, 1469-7645. doi: 10.1017/jfm.2018.770.

Charles Meneveau. Statistics of turbulence subgrid-scale stresses: Necessary conditions and experimental tests. *Phys. Fluids*, 6(2):815–833, 1994.

Parviz Moin. A new approach for large eddy simulation of turbulence and scalar transport. In *New Approaches and Concepts in Turbulence*, pages 331–339. Springer, 1993.

Vincent Mons, Yifan Du, and Tamer A. Zaki. Ensemble-variational assimilation of statistical data in large-eddy simulation. *Phys. Rev. Fluids*, 6(10):104607, October 2021. ISSN 2469-990X. doi: 10.1103/PhysRevFluids.6.104607.

Robert D Moser, Sigfried W Haering, and Gopal R Yalla. Statistical properties of subgrid-scale turbulence models. *Annu. Rev. Fluid Mech.*, 53(1):255–286, 2021.

Guido Novati, Hugues Lascombes De Laroussilhe, and Petros Koumoutsakos. Automating turbulence modelling by multi-agent reinforcement learning. *Nat. Mach. Intell.*, 3(1):87–96, January 2021. ISSN 2522-5839. doi: 10.1038/s42256-020-00272-0.

Paolo Orlandi. *Fluid Flow Phenomena: a Numerical Toolkit*, volume 55. Springer Science & Business Media, 2000.

Jonghwan Park and Haecheon Choi. Toward neural-network-based large eddy simulation: Application to turbulent channel flow. *J. Fluid Mech.*, 914:A16, May 2021. ISSN 0022-1120, 1469-7645. doi: 10.1017/jfm.2020.931.

Adam Paszke, Sam Gross, Francisco Massa, Adam Lerer, James Bradbury, Gregory Chanan, Trevor Killeen, Zeming Lin, Natalia Gimelshein, Luca Antiga, Alban Desmaison, Andreas Köpf, Edward Yang, Zach DeVito, Martin Raison, Alykhan Tejani, Sasank Chilamkurthy, Benoit Steiner, Lu Fang, Junjie Bai, and Soumith Chintala. Pytorch: An imperative style, high-performance deep learning library, 2019.

L. L. Pauley, P. Moin, and W. C. Reynolds. The structure of two-dimensional separation. *J. Fluid Mech.*, 220:397–411, 1990.

Sergio Pirozzoli, Davide Modesti, Paolo Orlandi, and Francesco Grasso. Turbulence and secondary motions in square duct flow. *J. Fluid Mech.*, 840:631–655, 2018.

Pierre Sagaut. *Large Eddy Simulation for Incompressible Flows: An Introduction*. Scientific Computation. Springer, Berlin, 3rd edition edition, 2006. ISBN 978-3-540-26344-9.

Benjamin Sanderse, Panos Stinis, Romit Maulik, and Shady E. Ahmed. Scientific machine learning for closure models in multiscale problems: A review. *Foundations of Data Science*, 7(1):298–337, 2025. doi: 10.3934/fods.2024043.

Varun Shankar, Dibyajyoti Chakraborty, Venkatasubramanian Viswanathan, and Romit Maulik. Differentiable turbulence: Closure as a partial differential equation constrained optimization. *Phys. Rev. Fluids*, 10(2):024605, 2025.

Claude E. Shannon. A mathematical theory of communication. *Bell Syst. Tech. J.*, 27(4):623–656, October 1948.

Juan A Sillero, Javier Jiménez, and Robert D Moser. One-point statistics for turbulent wall-bounded flows at reynolds numbers up to $\delta^+ \approx 2000$. *Phys. Fluids*, 25(10), 2013.

M. P. Simens, J. Jiménez, S. Hoyas, and Y. Mizuno. A high-resolution code for turbulent boundary layers. *J. Comp. Phys.*, 228(11):4218–4231, 2009.

Justin Sirignano and Jonathan F. MacArt. Deep learning closure models for large-eddy simulation of flows around bluff bodies. *J. Fluid Mech.*, 966:A26, July 2023. ISSN 0022-1120, 1469-7645. doi: 10.1017/jfm.2023.446.

Aaron Towne, Scott TM Dawson, Guillaume A Brès, Adrián Lozano-Durán, Theresa Saxton-Fox, Aadhy Parthasarathy, Anya R Jones, Hulya Biler, Chi-An Yeh, Het D Patel, et al. A database for reduced-complexity modeling of fluid flows. *AIAA J.*, 61(7):2867–2892, 2023.

Yunpeng Wang, Zelong Yuan, and Jianchun Wang. Ensemble data assimilation-based mixed subgrid-scale model for large-eddy simulations. *Phys. Fluids*, 35(8):085107, August 2023. ISSN 1070-6631, 1089-7666. doi: 10.1063/5.0160482.

Alan A Wray. Minimal storage time advancement schemes for spectral methods. *NASA Ames Research Center, California, Report No. MS*, 202, 1990.

Chenyue Xie, Jianchun Wang, Hui Li, Minping Wan, and Shiyi Chen. Artificial neural network mixed model for large eddy simulation of compressible isotropic turbulence. *Phys. Fluids*, 31(8):085112, August 2019. ISSN 1070-6631, 1089-7666. doi: 10.1063/1.5110788.

Lei Yang, Dong Li, Kai Zhang, Kun Luo, and Jianren Fan. Artificial neural-network-based subgrid-scale model for large-eddy simulation of isotropic turbulence. *Phys. Fluids*, 36(7), 2024.

Yuan Yuan and Adrián Lozano-Durán. Dimensionless learning based on information. *Nat. Commun.*, 16(1):9171, 2025.

Zelong Yuan, Yuepeng Wang, Xiaoning Wang, and Jianchun Wang. Adjoint-based variational optimal mixed models for large-eddy simulation of turbulence. *Phys. Fluids*, 35(7):075105, July 2023. ISSN 1070-6631, 1089-7666. doi: 10.1063/5.0155184.

Di Zhou and H Jane Bae. Sensitivity analysis of wall-modeled large-eddy simulation for separated turbulent flow. *J. Comput. Phys.*, 506:112948, 2024.

Di Zhou and H Jane Bae. Effect of subgrid-scale anisotropy on wall-modeled large-eddy simulation of separated flow. *arXiv preprint arXiv:2511.18566*, 2025.